Analytical calculation model for predicting cracking behavior of reinforced concrete ties

Tan, Reignard; Hendriks, Max A.N.; Geiker, Mette; Kanstad, Terje

DOI
10.1061/(ASCE)ST.1943-541X.0002510

Publication date
2020

Document Version
Final published version

Published in
Journal of Structural Engineering (United States)

Analytical Calculation Model for Predicting Cracking Behavior of Reinforced Concrete Ties

Reignard Tan, Ph.D.[1]; Max A. N. Hendriks[2]; Mette Geiker[3]; and Terje Kanstad[4]

Abstract: This paper formulates an analytical calculation model for predicting the cracking behavior of reinforced concrete ties to provide more consistent crack width calculation methods for large-scale concrete structures in which large bar diameters and covers are used. The calculation model was derived based on the physical behavior of reinforced concrete ties reported from experiments and finite-element analyses in the literature. The derivations led to a second order differential equation for the slip that accounts for the three-dimensional effects of internal cracking by using a proper bond-slip law. The second order differential equation for the slip was solved completely analytically, resulting in a closed-form solution in the case of lightly loaded members and in a non-closed-form solution in the case of heavily loaded members. Finally, the paper provides a solution strategy to facilitate a practical and applicable method for predicting the complete cracking response. Comparison with experimental and finite-element results in the literature demonstrated the ability of the calculation model to predict crack widths and crack spacing consistently and on the conservative side regardless of the bar diameter and cover. **DOI:** 10.1061/(ASCE)ST.1943-541X.0002510.

Author keywords: Crack widths; Crack distances; Analytical calculation model; Bond-slip; Reinforced concrete (RC) ties; Large-scale concrete structures.

Introduction

Predicting the cracking behavior of reinforced concrete (RC) structures consistently and accurately is not straightforward. This is reflected in the many approaches proposed in the literature (Borosnyói and Balázs 2005). Formulas based on empirical, semiempirical, elastic analysis, and even fracture mechanics have all been proposed. Mechanical calculation models based on the internal cracking behavior of RC ties have also recently been proposed (Fantilli et al. 2007; Debernardi and Taliano 2016; Kaklauskas 2017).

The study presented in this paper is part of an ongoing research project with the overall objective of improving crack width calculation methods for the large-scale concrete structures planned for the coastal highway route "Ferry-free E39" in Norway. The Norwegian Public Roads Administration (NPRA) recommends that the design of such structures should follow the guidelines provided in N400 (NPRA 2015), which state that the crack width calculation methods should be in accordance with the provisions in Eurocode 2 (EC2) (CEN 2004). However, Tan et al. (2018a) showed that the crack width formulas recommended by EC2 and the *fib* Model Code 2010 (MC2010) (*fib* 2013) predict the cracking behavior of structural elements inconsistently, particularly in cases of large covers and bar diameters. The analytical calculation model presented in this paper was based on solving the second order differential equation (SODE) for the slip when applying a bond-slip law first proposed by Eligehausen et al. (1983) and later adopted by MC2010. Other authors in the literature have used a similar approach (e.g., Russo and Romano 1992; Balázs 1993; Debernardi and Taliano 2016), an approach which has recently been acknowledged in the state-of-the-art French research project CEOS.fr (2016) as an alternative way of calculating crack widths for large RC members. The main drawback in using this approach until now was the analytically complex solution of the SODE for the slip, thus resorting to numerical solution techniques instead and by that reducing the practical applicability of the approach. Moreover, the background of the SODE for the slip was never properly elaborated.

The aim of this research was to provide more realistic and consistent surface crack width calculation methods for large-scale concrete structures, where large covers in combination with large bar diameters in several layers and bundles are typically used, by deriving and solving the SODE for the slip completely analytically. First, the SODE for the slip was derived. Then, the SODE for the slip was solved analytically, after which a solution strategy for determining the complete cracking response was developed for the purposes of practical application. Finally, the application was demonstrated by comparing analytical predictions with experimental and finite-element (FE) results reported in the literature.

The analytical model was derived using the concept of axisymmetry and applies first and foremost to such conditions. However, it will be shown that the model also has the ability to predict the cracking behavior of RC ties that deviate from such conditions by transforming an arbitrary cross section into an equivalent axisymmetric cross section. Moreover, predicting realistic and consistent surface crack widths is an important part of the structural design, and it might also be relevant for the aesthetics of a structure

[1]Structural Engineer, Dept. of Structural Engineering, Norwegian Univ. of Science and Technology, Trondheim 7491, Norway; Multiconsult AS, Postboks 265 Skøyen, Nedre Skøyen vei 2, Oslo 0213, Norway (corresponding author). ORCID: https://orcid.org/0000-0001-8190-6215. Email: reignard.tan@multiconsult.no

[2]Professor, Dept. of Structural Engineering, Norwegian Univ. of Science and Technology, Trondheim 7491, Norway; Assistant Professor, Faculty of Civil Engineering and Geosciences, Delft Univ. of Technology, 2628 CN Delft, Netherlands. ORCID: https://orcid.org/0000-0001-9507-3736

[3]Professor, Dept. of Structural Engineering, Norwegian Univ. of Science and Technology, Trondheim 7491, Norway.

[4]Professor, Dept. of Structural Engineering, Norwegian Univ. of Science and Technology, Trondheim 7491, Norway.

Note. This manuscript was submitted on April 16, 2018; approved on June 17, 2019; published online on December 12, 2019. Discussion period open until May 12, 2020; separate discussions must be submitted for individual papers. This paper is part of the ***Journal of Structural Engineering***, © ASCE, ISSN 0733-9445.

(Leonhardt 1988). On the other hand it is often argued that the crack width at the reinforcement appears more relevant in terms of durability. Predicting the latter, though, becomes rather complicated and was not addressed in this study.

Physical Behavior of RC Ties

A typical deformation configuration of RC ties according to several experimental studies reported in the literature (Watstein and Mathey 1959; Broms 1968; Husain and Ferguson 1968; Yannopoulos 1989; Beeby 2004; Borosnyói and Snóbli 2010) is depicted in Fig. 1(a). Note that the crack width at the interface between concrete and steel $w_{\mathrm{cr,int}}$ is considerably smaller than that on the concrete surface w_{cr}, which according to Goto (1971) and Tammo and Thelandersson (2009) is due to the rib interaction between concrete and steel. This causes the concrete to crack internally, which allows it to follow the displacement field of steel at the interface almost completely. This reported physical behavior formed the basis for ignoring the crack width at the interface in the FE model of Tan et al. (2018b). This imposed equal longitudinal displacements for concrete and steel at the interface as shown in Fig. 1(b), in which it should be noted that the crack width w_{cr} applies to the concrete surface only. The FE model was validated against the classical experiments of Bresler and Bertero (1968) and Yannopoulos (1989), where comparison of steel strains, the development of crack widths and the mean crack spacing showed good agreement. Furthermore, the FE model was also used to analyze cylindrical RC ties to better understand the cracking behavior. It was observed that the bond transfer at the interface caused radial displacements of the concrete, which in turn increased hoop stresses and strains. This resulted in internal splitting cracks and inclined cracks, depicted respectively as circles and straight lines in Fig. 1(b), when the principal stresses exceeded the tensile strength of the concrete. Moreover, deriving local bond-slip curves at different positions over the bar length showed that

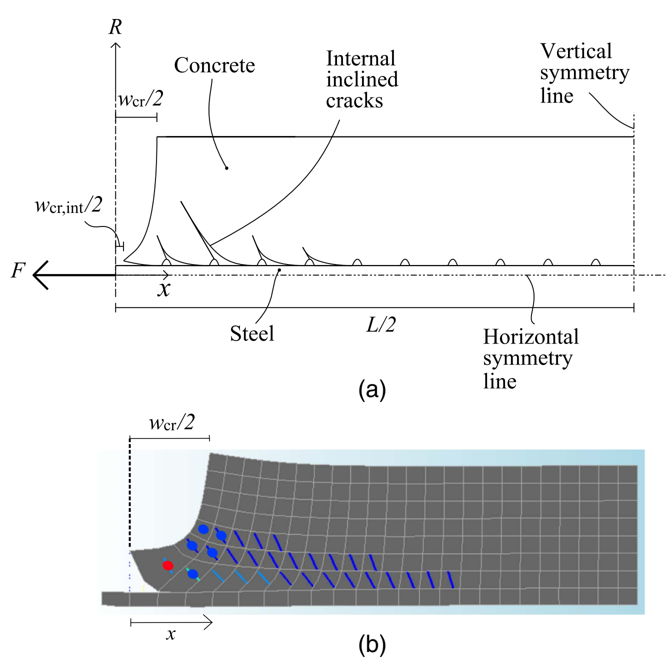

Fig. 1. (a) Typical deformation configuration of RC ties with deformed steel bars observed in experiments; and (b) FE model with assumptions in accordance with Tan et al. (2018b) showing a typical deformation configuration and crack plot, where straight lines indicate inclined internal cracks and circles indicate internal splitting cracks.

such curves include the effect that internal splitting and inclined cracks had on reducing the bond transfer. In other words, the local bond-slip curve describes how the 3D behavior of an RC tie affects the bond transfer. This shows that a single local bond-slip curve is sufficient to describe the mean bond transfer at the interface between concrete and steel for an arbitrary RC tie.

Mechanical Crack Width Calculation Model

Main Assumptions

The analytical calculation model was derived based on the physical behavior of RC ties discussed in the previous section. However, some simplifications were made, and at first the concept of axisymmetry was also used for simplicity. Firstly, concrete and steel were both treated as elastic materials. Secondly, the nonlinearity of the internal cracking of the confining concrete was accounted for by lumping this behavior to the interface between the materials using a bond-slip law, i.e., claiming that the three sections in Figs. 2(a–c) are statically equivalent. Note that a physical slip u occurs at the interface in Figs. 2(b and c) as a result of treating concrete and steel as elastic materials. This means that the total slip s_{tot} in the statically equivalent section in Fig. 2(c) is composed of two parts: the slip at the interface u caused by the formation of internal inclined cracks and the elastic deformations of the concrete caused by axial and shear deformations in the cover s_{s}. This also conforms to the definition of slip in *fib* bulletin 10 (*fib* 2000). Assuming that the slip at the interface is equivalent to the deformation caused by internal inclined cracks implies in reality that the crack width at the interface can be ignored in the calculation model, so that the resulting crack width applies to the concrete surface. Furthermore, the Poisson's ratio for concrete can be ignored ($\nu_{\mathrm{c}} = 0$) because the concrete is assumed to be exposed to heavy internal cracking as described in the previous section. Finally, the displacement field depicted in Fig. 3, which shows the deformed configuration of an arbitrary section in an RC tie subjected to loading at the rebar ends, can be assumed to apply for an arbitrary statically equivalent section.

The continuum concept (Irgens 2008) is hereafter used to formulate the compatibility, material laws, and equilibrium for concrete and steel.

Equations for Concrete

General Equations

The SODE for the concrete displacements was derived by using the cylindrical coordinates and the displacement field depicted in Fig. 3. Concrete strains at the interface $\varepsilon_{\mathrm{ci}}$ and the specimen surface $\varepsilon_{\mathrm{co}}$ were assumed to be related as

$$\psi(x) = \frac{\varepsilon_{\mathrm{co}}}{\varepsilon_{\mathrm{ci}}} \leq 1 \tag{1}$$

in which

$$\varepsilon_{\mathrm{ci}} = \frac{dw_{\mathrm{ci}}(x)}{dx} \tag{2}$$

and

$$\varepsilon_{\mathrm{co}} = \frac{dw_{\mathrm{co}}(x)}{dx} \tag{3}$$

where dw_{ci} and dw_{co} are differential displacements at the interface and at the specimen surface respectively. Note that the inequality in Eq. (1) is because the concrete strains at the specimen surface

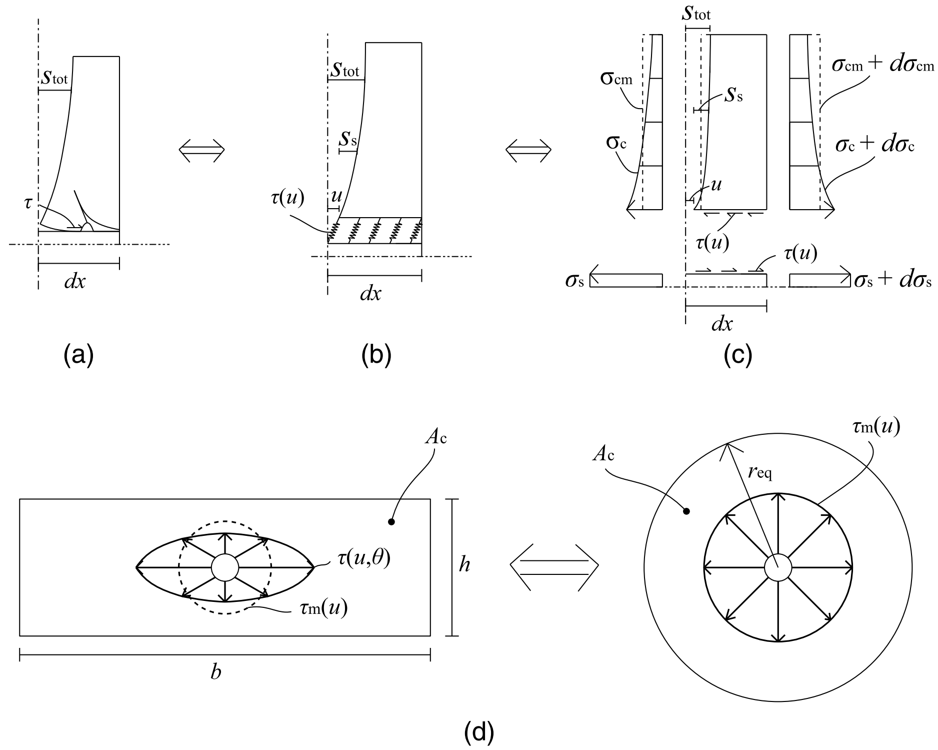

Fig. 2. (a) Internally cracked section typically observed in physical experiments; (b) the internal cracking behavior lumped as springs to the interface between concrete and steel; (c) statically equivalent section using a bond-slip law for the springs; and (d) equivalent cross sections when using the second order differential equation for the slip.

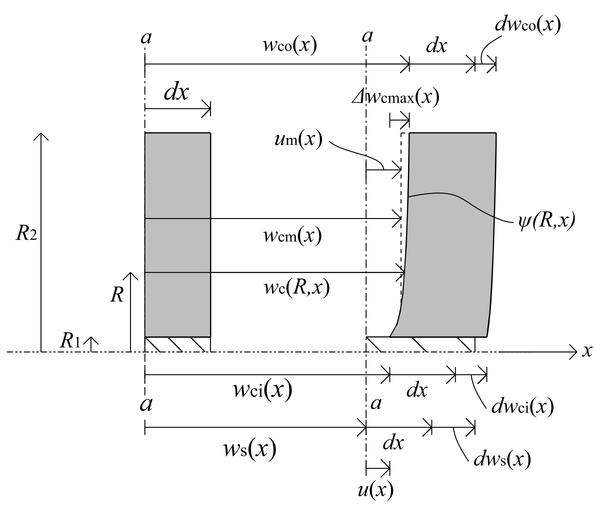

Fig. 3. Displacement field of an arbitrary statically equivalent section. The section to the left-hand side shows the undeformed configuration, while the section to the right-hand side shows the deformed configuration for a load applied to the rebar end greater than zero.

cannot exceed the concrete strains at the interface as a consequence of force being applied at the steel bar ends. The maximum longitudinal displacement of the concrete cover relative to the concrete interface is

$$-\Delta w_{\mathrm{cmax}}(x) = w_{\mathrm{ci}}(x) - w_{\mathrm{co}}(x) \tag{4}$$

Moreover, longitudinal concrete displacements can be formulated as

$$w_{\mathrm{c}}(R,x) = w_{\mathrm{ci}}(x) + \Delta w_{\mathrm{cmax}}(x)\bar{\psi}(R,x) \tag{5}$$

in which $\bar{\psi}$ is a shape function describing the variation in longitudinal displacements over the section and over the bar length. It was chosen to satisfy the following boundary conditions:

$$w_{\mathrm{c}}(R_1,x) = w_{\mathrm{ci}}(x)$$
$$w_{\mathrm{c}}(R_2,x) = w_{\mathrm{co}}(x) \tag{6}$$

where R_1 and R_2 are the radial coordinates of respectively the interface and the specimen surface. It should be noted that Fig. 3 omits radial displacements for the concrete, while in the case of axisymmetry displacements in the hoop direction are nonexistent. Omitting radial displacements contradicts the physical behavior of RC ties discussed previously, but using a bond-slip law $\tau(u)$, with τ denoting the bond stress, will take into account the 3D effects that are excluded when radial displacements for the concrete are omitted. This means that Eq. (5) suffices in describing the displacement field for concrete. Now, using Green strains for small displacements yield the following nonzero components in the strain tensor for concrete:

$$\varepsilon_{\mathrm{c}} = \frac{\partial w_{\mathrm{c}}(R,x)}{\partial x} = \frac{dw_{\mathrm{ci}}(x)}{dx} + \frac{\partial}{dx}[\Delta w_{\mathrm{cmax}}(x)\bar{\psi}(R,x)] \tag{7}$$

$$\gamma_{\mathrm{c}Rx} = \gamma_{\mathrm{c}xR} = \frac{\partial w_{\mathrm{c}}(R,x)}{\partial R} = \Delta w_{\mathrm{cmax}}(x)\frac{d\bar{\psi}(R,x)}{dR} \tag{8}$$

where ε_{c} and $\gamma_{\mathrm{c}Rx} = \gamma_{\mathrm{c}xR}$ are longitudinal strains and engineering shear strains respectively. Consequently, Eqs. (7) and (8), and ignoring the Poisson's ratio for concrete, yield the following nonzero components for the stress tensor:

$$\sigma_{\mathrm{c}} = E_{\mathrm{c}}\varepsilon_{\mathrm{c}} \tag{9}$$

$$\tau_{cxR} = \tau_{cRx} = \frac{1}{2} E_c \gamma_{cxR} \quad (10)$$

where σ_c and $\tau_{cRx} = \tau_{cxR}$ are respectively the normal and the shear stresses, while E_c is the Young's modulus for concrete. Considering equilibrium for the concrete in Fig. 2(c) yields

$$\frac{dF_c(x)}{dx} = \tau(u) \sum \pi\phi_s \quad (11)$$

where τ is the bond stress dependent on the slip at the interface u, and $\sum \pi\phi_s$ is the total perimeter surrounding the steel bars in a cross section. The concrete force resultant can be formulated as

$$F_c(x) = \int_{A_c} \sigma_c dA_c \quad (12)$$

where A_c is the concrete area.

Finally, inserting Eqs. (12), (9), (7), (4), (1), (2), and (3) in Eq. (11) successively yields

$$E_c \frac{\partial}{\partial x} \int_{A_c} \left\{ \frac{dw_{ci}(x)}{dx} - \frac{dw_{ci}(x)}{dx} [1 - \psi(x)] \bar{\psi}(R, x) - [w_{ci}(x) - w_{co}(x)] \frac{\partial \bar{\psi}(R, x)}{\partial x} \right\} dA_c = \tau(u) \sum \pi\phi_s \quad (13)$$

which is the SODE for the longitudinal concrete displacements at the interface.

Simplified Equations

An analytical solution of Eq. (13) is possible in the case of axisymmetry if both ψ and $\bar{\psi}$ are known. In most practical situations, however, this is not the case. A practical approach to Eq. (13) would therefore be to redefine Eq. (1) as

$$\psi(x) = \psi = \frac{\varepsilon_{cm}}{\varepsilon_{ci}} \leq 1 \quad (14)$$

in which

$$\varepsilon_{cm} = \frac{dw_{cm}(x)}{dx} = \psi \varepsilon_{ci} \quad (15)$$

are mean concrete strains and w_{cm} are mean displacements over the section—see Fig. 3, which in this particular case simplifies the shape function to

$$\bar{\psi} = 1 \quad (16)$$

Note that ψ in Eq. (14) is now assumed constant. Edwards and Picard (1972) were the first to introduce the concept of Eq. (14). This was later investigated more thoroughly by conducting nonlinear finite-element analysis (NLFEA) on cylindrical RC ties in Tan et al. (2018c). It was concluded that although the shape function $\bar{\psi}$, first defined in Eq. (5) varied with respect to both R and x-coordinates over the bar length, the ratio in Eq. (14) remained more or less constant over the bar length except for a small region close to the loaded end. Actually, it was observed that a constant value of $\psi = 0.70$ over the entire bar length seemed reasonable independent of geometry and load level. The physical interpretation of Eq. (15) is that *plane sections that do not remain plane* are implicitly accounted for in determining the equilibrium. Now, replacing w_{co} with w_{cm} in Eq. (13) and inserting Eqs. (14) and (16) simplifies the SODE for the longitudinal concrete displacements at the interface to

$$\psi A_c E_c \frac{d^2 w_{ci}(x)}{dx^2} = \tau(u) \sum \pi\phi_s \quad (17)$$

Equations for Steel

Longitudinal displacements for steel were assumed uniform over its radius. And since the Poisson's ratio for concrete was ignored and axisymmetry applied for circular steel rebars means that Eq. (18)

$$w_s(R, x) = w_s(x) \quad (18)$$

suffices in describing the displacement field for steel. The following normal strain was thus the only nonzero component in the strain tensor when Green strains for small deformations were applied:

$$\varepsilon_s = \frac{dw_s(x)}{dx} \quad (19)$$

Moreover, the Poisson's ratio for steel was ignored ($\nu_s = 0$) as the lateral effects it had on bond were assumed to be included in the bond-slip curve. This led to the following normal stress being the only nonzero component in the stress tensor:

$$\sigma_s = E_s \varepsilon_s \quad (20)$$

where E_s is the Young's modulus for steel. The equilibrium of steel in Fig. 2(c) yields

$$\frac{dF_s(x)}{dx} = -\tau(u) \sum \pi\phi_s \quad (21)$$

Furthermore, the steel force resultant was obtained as

$$F_s(x) = \int_{A_s} \sigma_s dA_s = A_s E_s \frac{dw_s(x)}{dx} \quad (22)$$

when inserting Eqs. (20) and (19) successively. Finally, inserting Eqs. (22) in (21) yields

$$A_s E_s \frac{d^2 w_s(x)}{dx^2} = -\tau(u) \sum \pi\phi_s \quad (23)$$

which is the SODE for the steel displacements.

Compatibility

The slip was defined in terms of the displacement field depicted in Fig. 3 as

$$-u(x) = w_s(x) - w_{ci}(x) \quad (24)$$

Differentiating Eq. (24) once and inserting Eqs. (2) and (19) provides the first derivative of the slip as

$$-u'(x) = \frac{dw_s(x)}{dx} - \frac{dw_{ci}(x)}{dx} = \varepsilon_s - \varepsilon_{ci} \quad (25)$$

Second Order Differential Equation for the Slip

Inserting Eq. (23) in (17) provides

$$\frac{d}{dx}\left[\frac{dw_{ci}(x)}{dx} + \xi \frac{dw_s(x)}{dx}\right] = 0 \quad (26)$$

where

$$\xi = \frac{\alpha_e \rho_s}{\psi} \quad (27)$$

$$\alpha_e = \frac{E_s}{E_c} \quad (28)$$

and

$$\rho_s = \frac{A_s}{A_c} \tag{29}$$

Inserting Eqs. (25) and (23) successively in Eq. (26) yields the SODE for the slip as

$$\frac{d^2u(x)}{dx^2} - \chi\tau(u) = 0 \tag{30}$$

where

$$\chi = \frac{\sum \pi\phi_s}{A_s E_s}(1+\xi) \tag{31}$$

By introducing

$$\zeta = \frac{\tau_m(u)}{\tau(u,\theta)} \leq 1 \tag{32}$$

where τ_m and $\tau(u,\theta)$ is respectively the mean and the maximum bond stress around the circumference of a steel bar in an arbitrary cross section, and further multiplying χ in Eq. (30) by ζ from Eq. (32) takes into account the bond stress τ not being constant around the circumference of the steel bar in nonaxisymmetric cases, such as when the cover to the steel surface varies in a cross section as depicted in Fig. 2(d). In practice, this implies taking the distance between rebars into account, a parameter acknowledged by the research of Gergely and Lutz (1968) to be significant for the crack width. This means that the solution of Eq. (30) with χ multiplied by ζ from Eq. (32) involves transforming a cross section with an arbitrary geometry into a circular cross section with a radius r_{eq} such that the area A_c remains the same.

The analytical solution of Eq. (30) depends on the choice of the bond-slip law and a variety of choices can be found in the literature (Rehm 1961; Nilson 1972; Martin 1973; Dörr 1978; Mirza and Houde 1979; Hong and Park 2012). In this study, the local bond-slip law recommended by MC2010 was used:

$$\tau(u) = \tau_{max}\left(\frac{u}{u_1}\right)^{\alpha} \tag{33}$$

Eq. (33) and its parameters were originally derived on the basis of pull-out tests of relatively short specimens, in which the concrete was in compression, thus differing considerably from the stress conditions in RC ties where the concrete is in tension (Pedziwiatr 2008). However, the investigation by Tan et al. (2018b) showed that Eq. (33) could be applied to represent the mean bond transfer over the specimen length by using the predefined parameters $\tau_{max} = 5.0$ MPa, $u_1 = 0.1$, and $\alpha = 0.35$ when comparing it to the local bond-slip curves obtained from the FE analysis of several RC ties, see Fig. 4. Bond-slip curves proposed by other authors are also shown in the same figure. This means that inserting Eq. (33) in Eq. (30) finally yields the SODE

$$\frac{d^2u}{dx^2} - \chi\frac{\tau_{max}}{u_1^{\alpha}}u^{\alpha} = 0 \tag{34}$$

Note that Eq. (34) has been derived and will be solved using the simplified equations for concrete.

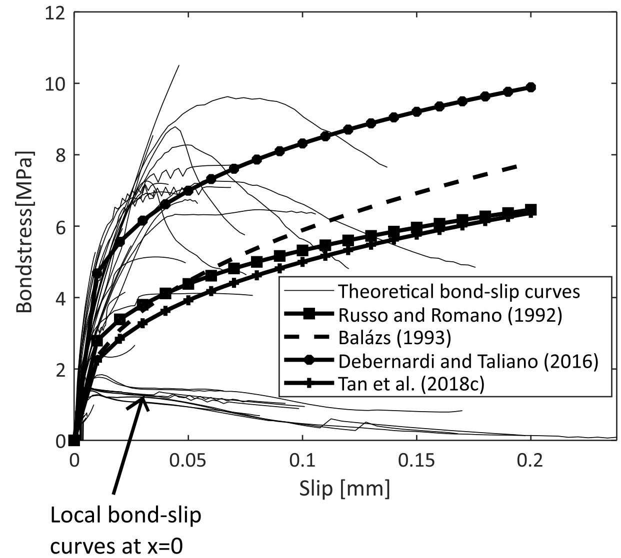

Fig. 4. Local bond-slip curves according to Eq. (33) with adjusted parameters proposed by Russo and Romano (1992), Balázs (1993), Debernardi and Taliano (2016), and Tan et al. (2018b) compared with theoretical local bond-slip curves obtained in the FE analysis of several RC ties at different positions over the bar length in Tan et al. (2018b).

Analytical Crack Width Calculation Model

General Solutions

Slip

Eq. (34) is a nonlinear homogenous SODE and can be solved analytically, by successively defining the second term as a function of the slip $f(u)$, moving it to the other side of the equals sign, multiplying both sides with the first derivative of the slip u', applying the chain rule on the left-hand side of the equal sign and the substitution rule on the right-hand side, and subsequently integrating once, the first derivative of the slip is provided as

$$u' = \frac{du}{dx} = -\sqrt{2(\gamma u^{\beta} + C)} \tag{35}$$

where C is an integration constant and

$$\beta = 1 + \alpha \tag{36}$$

and

$$\gamma = \chi\frac{\tau_{max}}{\beta u_1^{\alpha}} \tag{37}$$

Only the negative sign is included in Eq. (35) for compatibility with Eq. (25). Separating the variables in Eq. (35) and integrating on both sides yields

$$x = B - \frac{1}{\sqrt{2}}\int (\gamma u^{\beta} + C)^{-\frac{1}{2}} du \tag{38}$$

where B is an integration constant. The integral can now be solved using the method proposed by Russo et al. (1990) and Russo and Romano (1992) where the binomial in Eq. (38) is developed as an infinite series of functions in accordance with Newton's binomial theorem and then integrating each term. This results in two different general solutions that converge at distinct intervals

J. Struct. Eng., 2020, 146(2): 04019206

$$x = B_1 - \frac{1}{\sqrt{2}} \sum_{k=0}^{\infty} \binom{-\frac{1}{2}}{k} \gamma^k \left(\frac{1}{C}\right)^{\left(\frac{1}{2}+k\right)} \frac{u^{1+k\beta}}{1+k\beta} \quad \text{for } 0 < u < u_d \tag{39}$$

and

$$x = B_2 - \frac{1}{\sqrt{2\gamma}} \sum_{k=0}^{\infty} \binom{-\frac{1}{2}}{k} \left(\frac{C}{\gamma}\right)^k \frac{u^{\delta-k\beta}}{\delta-k\beta} \quad \text{for } u > u_d \tag{40}$$

where B_1 and B_2 are integration constants, and

$$\delta = \frac{1-\alpha}{2} \tag{41}$$

while

$$u_d = \left|\frac{C}{\gamma}\right|^{\frac{1}{\beta}} \tag{42}$$

is the value discerning Eq. (39) from (40). Note that the general solutions in Eqs. (39) and (40) imply that the longitudinal coordinate x is a function of the slip value u as a consequence of splitting the variables in Eq. (35).

Strains

Successively inserting Eqs. (2) and (19) in Eq. (26), integrating once, and applying $\varepsilon_{ci} = 0$ and $\varepsilon_s = F/E_s A_s = \varepsilon_{s0}$ at the loaded end (i.e., at $x = 0$) yields

$$\varepsilon_{ci} = \xi(\varepsilon_{s0} - \varepsilon_s) \tag{43}$$

Inserting Eqs. (35) and (43) in Eq. (25) yields the steel strains

$$\varepsilon_s = \frac{\xi\varepsilon_{s0} + \sqrt{2(\gamma u^\beta + C)}}{1+\xi} \tag{44}$$

while inserting Eqs. (44) in (43) provides the concrete strains

$$\varepsilon_{ci} = \xi \frac{\varepsilon_{s0} - \sqrt{2(\gamma u^\beta + C)}}{1+\xi} \tag{45}$$

Boundary Conditions

Boundary conditions must be established before calculating particular solutions. These are established by considering the concepts of *comparatively lightly loaded members* (CLLM) and *comparatively heavily loaded members* (CHLM) depicted in Fig. 5. Russo and Romano (1992) were the first to introduce these concepts, which were later acknowledged by *fib* bulletin 10 (*fib* 2000). Briefly summarized, the main difference is that steel and concrete strains become compatible, $\varepsilon_s = \varepsilon_{ci}$, at a certain distance x_r from the loaded end in the case of CLLM, while the strains remain incompatible, $\varepsilon_s \neq \varepsilon_{ci}$, over the entire bar length in the case of CHLM. This further implies, in accordance with Eq. (24), that the slip becomes zero at distance x_r from the loaded end in the case of CLLM and at the symmetry section x_S in the case of CHLM. This yields the following boundary conditions in the case of CLLM behavior:

$$\begin{aligned} -u_r &= 0 \\ -u'_r &= \varepsilon_s - \varepsilon_{ci} = 0 \end{aligned} \tag{46}$$

at $x = x_r$, and in the case of CHLM behavior:

$$\begin{aligned} -u_S &= 0 \\ -u'_S &= \varepsilon_s - \varepsilon_{ci} > 0 \end{aligned} \tag{47}$$

at $x = x_S = (L/2)$.

CLLM

Applying the boundary conditions in Eq. (46) for Eq. (35) yields

$$C = 0 \tag{48}$$

Inserting Eq. (48) in (38), integrating once, and applying the boundary conditions in Eq. (46) again yields the expression for the slip in the case of CLLM behavior

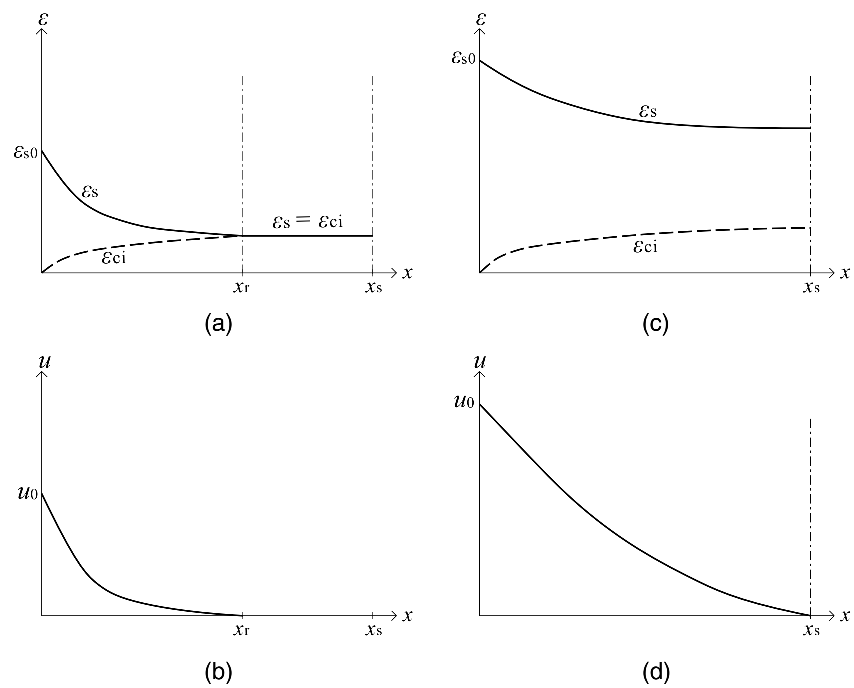

Fig. 5. (a and b) Strain and slip distribution in CLLM; and (c and d) strain and slip distribution in CHLM.

$$u = \left[\delta\sqrt{2\gamma}(x_r - x)\right]^{\frac{1}{\delta}} \tag{49}$$

Inserting Eq. (48) in (44) and acknowledging that $\varepsilon_s = \varepsilon_{s0}$ at $x = 0$, provides the maximum slip at the loaded end as

$$u_0 = \left(\frac{\varepsilon_{s0}^2}{2\gamma}\right)^{\frac{1}{\beta}} \tag{50}$$

Furthermore, inserting Eq. (50) in (49) for $x = 0$ yields the transfer length as

$$x_r = \frac{1}{\delta}\left[\varepsilon_{s0}\left(\frac{1}{2\gamma}\right)^{\frac{1}{2\delta}}\right]^{\frac{2\delta}{\beta}} \tag{51}$$

Note that the transfer length increases with increasing steel strains $\varepsilon_{s0} = F/E_sA_s$ at the loaded end. Expressions for the steel and concrete strains can be finally obtained by inserting Eq. (49) in respectively Eqs. (44) and (45):

$$\varepsilon_s = \frac{\xi\varepsilon_{s0} + (2\gamma)^{\frac{1}{2\delta}}[\delta(x_r - x)]^{\frac{\beta}{2\delta}}}{1+\xi} \tag{52}$$

$$\varepsilon_{ci} = \xi\frac{\varepsilon_{s0} - (2\gamma)^{\frac{1}{2\delta}}[\delta(x_r - x)]^{\frac{\beta}{2\delta}}}{1+\xi} \tag{53}$$

One application of the particular solutions obtained could be in the case of two consecutive cracks formed with a considerable distance between them. This means that a certain region, $2(x_s - x_r)$, remains undisturbed as depicted in Figs. 5(a and b). This situation occurs typically in the so-called *crack formation stage*, in which the applied member load is relatively low and the distance between two consecutive cracks formed is relatively large.

CHLM

Particular Solutions

Applying the boundary conditions in Eq. (47) in (35) yields

$$u_s' = -\sqrt{2C} \tag{54}$$

Acknowledging from Eq. (35) and Fig. 5 that u' is a real function yields

$$C > 0 \tag{55}$$

This means that the general solutions of Eqs. (39) and (40) apply in the case of CHLM because $C \neq 0$. Now, inserting Eq. (35) in (25) and applying $\varepsilon_{ci} = 0$ and $\varepsilon_s = F/E_sA_s = \varepsilon_{s0}$ at the loaded end (i.e., at $x = 0$) yields

$$C = \frac{\varepsilon_{s0}^2}{2} - \gamma u_0^\beta \tag{56}$$

Furthermore, Eqs. (55) and (56) imply that the maximum slip at the loaded end must satisfy

$$u_{0,\max} = \left(\frac{\varepsilon_{s0}^2}{2\gamma}\right)^{\frac{1}{\beta}} \tag{57}$$

Inserting Eq. (56) in (42) and acknowledging that Eq. (37) is a positive value provides

$$u_d = \left(\frac{\varepsilon_{s0}^2}{2\gamma} - u_0^\beta\right)^{\frac{1}{\beta}} \tag{58}$$

Now, applying the first condition in Eq. (47) to (39) yields

$$B_1 = \frac{L}{2} \tag{59}$$

Moreover, applying $u = u_0$ at $x = 0$ for Eq. (40) yields that B_2 can be expressed with binomial coefficients as

$$B_2 = \frac{1}{\sqrt{2\gamma}}\sum_{k=0}^{\infty}\binom{-\frac{1}{2}}{k}\left(\frac{C}{\gamma}\right)^k\frac{u_0^{\delta-k\beta}}{\delta-k\beta} \tag{60}$$

The particular solutions of Eqs. (39) and (40) are now obtained using the integration constants in Eqs. (56), (59), and (60). It should be noted, however, that the integration constants in Eqs. (56) and (60) depend on the slip at the loaded end u_0, so they must be obtained iteratively. This can be done conveniently by considering the two cases shown in Fig. 6.

Case 1

The first case involves solving Eq. (39) with respect to the slip at the loaded end in its interval when $u_0 < u_d$ in accordance with Fig. 6(a). Inserting Eq. (59) in (39) and applying $u = u_0$ at $x = 0$ provides the function

$$f_1(u_0) = \frac{L}{2} - \frac{1}{\sqrt{2}}\sum_{k=0}^{\infty}\binom{-\frac{1}{2}}{k}\gamma^k\left(\frac{1}{C}\right)^{\left(\frac{1}{2}+k\right)}\frac{u_0^{1+\beta k}}{1+\beta k} = 0 \tag{61}$$

which is valid for the interval

$$0 \leq u_0 < \left(\frac{\varepsilon_{s0}^2}{4\gamma}\right)^{\frac{1}{\beta}} \tag{62}$$

when acknowledging that u_d in Eq. (39) is given by Eq. (58).

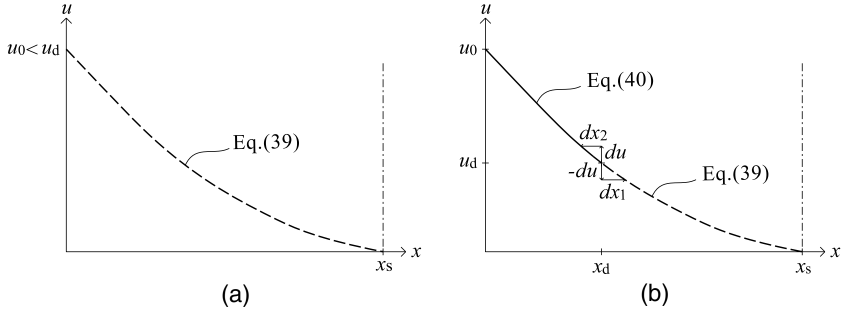

Fig. 6. (a) Case 1: solution for the slip using Eq. (39), i.e., $u_0 < u_d$; and (b) Case 2: solution for the slip using Eq. (39) for $0 < u < u_d$ and Eq. (40) for $u_d < u < u_0$.

Case 2

Case 2 is where $u_0 > u_d$, which means that the solution for the slip u depends on both Eqs. (39) and (40) due to the validity of the equations at its respective intervals—see Fig. 6(b). In other words, Eq. (39) is valid for slip values below u_d while Eq. (40) is valid for slip values above u_d. Now, accepting that Eq. (39) is valid for the slip value $u = u_\mathrm{d} - du$ at the location $x_\mathrm{d} + dx_1$ provides

$$x_\mathrm{d} + dx_1 = \frac{L}{2} - \frac{1}{\sqrt{2}} \sum_{k=0}^{\infty} \binom{-\frac{1}{2}}{k} \gamma^k \left(\frac{1}{C}\right)^{\left(\frac{1}{2}+k\right)} \frac{(u_\mathrm{d} - du)^{1+\beta k}}{1+\beta k} \tag{63}$$

Similarly, accepting that Eq. (40) is valid for the slip value $u = u_\mathrm{d} + du$ at the location $x_\mathrm{d} - dx_2$ and inserting Eq. (60) provides

$$\begin{aligned} x_\mathrm{d} - dx_2 = {} & \frac{1}{\sqrt{2\gamma}} \sum_{k=0}^{\infty} \binom{-\frac{1}{2}}{k} \left(\frac{C}{\gamma}\right)^k \frac{u_0^{\delta-k\beta}}{\delta - k\beta} \\ & - \frac{1}{\sqrt{2\gamma}} \sum_{k=0}^{\infty} \binom{-\frac{1}{2}}{k} \left(\frac{C}{\gamma}\right)^k \frac{(u_\mathrm{d} + du)^{\delta-k\beta}}{\delta - k\beta} \end{aligned} \tag{64}$$

Note that du is an infinitesimal value for the slip, while dx_1 and dx_2 are infinitesimal values along the bar length in accordance with Fig. 6(b). Subtracting Eq. (64) from (63) provides the function

$$f_2(u_0) = \frac{L}{2} - \frac{1}{\sqrt{2\gamma}} \{f_{21}(u_0) - f_{22}(u_0)\} - \frac{1}{\sqrt{2}} f_{23}(u_0) - \Delta x = 0 \tag{65}$$

where

$$f_{21}(u_0) = \sum_{k=0}^{\infty} \binom{-\frac{1}{2}}{k} \left(\frac{C}{\gamma}\right)^k \frac{u_0^{\delta-k\beta}}{\delta - k\beta} \tag{66}$$

$$f_{22}(u_0) = \sum_{k=0}^{\infty} \binom{-\frac{1}{2}}{k} \frac{\left[\left(\frac{C}{\gamma}\right)^{\frac{k}{\delta-k\beta}+\frac{1}{\beta}} + du\left(\frac{C}{\gamma}\right)^{\frac{k}{\delta-k\beta}}\right]^{\delta-k\beta}}{\delta - k\beta} \tag{67}$$

$$f_{23}(u_0) = \sum_{k=0}^{\infty} \binom{-\frac{1}{2}}{k} \frac{\gamma^k \left[C^{\frac{2-\beta}{2\beta(1+k\beta)}} \left(\frac{1}{\gamma}\right)^{\frac{1}{\beta}} - du\, C^{-\frac{\frac{1}{2}+k}{1+k\beta}}\right]^{1+k\beta}}{1+k\beta} \tag{68}$$

and $\Delta x = dx_1 + dx_2$. Eq. (65) is valid for

$$u_0 > \left(\frac{\varepsilon_{s0}^2}{4\gamma}\right)^{\frac{1}{\beta}} \tag{69}$$

when acknowledging that u_d in Eq. (40) is given by Eq. (58).

Solution Strategy

Russo and Romano (1992) give a convenient way of determining whether Case 1 or Case 2 governs by calculating Eq. (61) for a value of u_0 close to the upper limit value in Eq. (62), e.g., as $u_{0\mathrm{check}} = (\varepsilon_{s0}^2/4\gamma - du)^{1/\beta}$. Case 1 governs if the value calculated is negative. Case 2 governs if the value calculated is positive since the nature of Eq. (61) invokes that u_0 must increase to satisfy Eq. (61), which implies that Eq. (69) governs.

Newton-Raphson iterations are used to calculate the value of u_0 effectively after determining whether Case 1 or 2 governs

$$u_{0,i+1} = u_{0,i} - \frac{f_j(u_{0,i})}{f_j'(u_{0,i})} \tag{70}$$

where index i represents the number of iterations and index j represents the function in Eq. (61) for Case 1 or Eq. (65) for Case 2. Furthermore, it is suggested that an initial value of $u_{0,\mathrm{init}} = (\varepsilon_{s0}^2/4\gamma)^{1/\beta} - du$ is used for Case 1 or $u_{0,\mathrm{init}} = (\varepsilon_{s0}^2/4\gamma)^{1/\beta} + du$ is used for Case 2 to start the iterations in Eq. (70). The iterated value $u_{0,i+1}$, however, should never exceed Eq. (57) due to the requirement of Eq. (55). Convergence is achieved when $|u_{0,i+1} - u_{0,i}| < Tol$, at which Tol is a chosen tolerance value. Note that the derivatives of the functions in Eqs. (61) and (65) are needed to solve Eq. (70) and are provided in Appendix I. Once the value of u_0 is obtained, the particular solutions of Eqs. (39) and (40) are used to obtain the corresponding x values for the slip u along the bar length. In summary, CHLM involves determining whether Case 1 or 2 governs using Eq. (61) before the slip at the loaded end u_0 is calculated using Eq. (70).

Strains

The strain distributions for steel and concrete were obtained by using Eqs. (44) and (45) respectively. Moreover, inserting Eq. (45) in (15), and acknowledging that the maximum concrete strains will occur at the symmetry section (i.e., where the slip $u = 0$) provides the maximum mean concrete strains as

$$\varepsilon_{\mathrm{cm,max}} = \psi\xi \frac{\varepsilon_{s0} - \sqrt{2C}}{1+\xi} < \varepsilon_{\mathrm{ct}} \tag{71}$$

The violation of Eq. (71) implies that a crack has formed at the symmetry section, meaning a new member with length $L/2$ exists and that the CHLM response should be determined for the newly formed member.

Conditions at Crack Formation

The conditions at crack formation are shown in Fig. 7, where the transfer length increases with increasing load as highlighted for Eq. (51). The steel strain at the loaded end needed to extend the transfer length to the symmetry section is obtained by inserting $x_\mathrm{r} = L/2$ in Eq. (51) so that

$$\varepsilon_{\mathrm{s0,S}} = (2\gamma)^{\frac{1}{2\delta}} \left(\frac{L}{2}\delta\right)^{\frac{\beta}{2\delta}} \tag{72}$$

Furthermore, the maximum mean concrete strain at the end of the transfer length x_r is obtained by inserting Eq. (53) in (15) at $x = x_\mathrm{r}$ so that

$$\varepsilon_{\mathrm{cm,max}} = \frac{\psi\xi}{1+\xi} \varepsilon_{s0} \tag{73}$$

It is assumed that a crack forms when $\varepsilon_{\mathrm{cm,max}} = \varepsilon_{\mathrm{ct}}$, which means that the corresponding steel strain at the loaded end is

$$\varepsilon_{\mathrm{s0,cr}} = \varepsilon_{\mathrm{ct}} \frac{1+\xi}{\psi\xi} \tag{74}$$

So inserting Eq. (74) in (51) yields the distance from the loaded end at which a new crack can form or, expressed more rigorously, the *crack spacing*

$$x_{\mathrm{cr}} = \frac{1}{\delta} \left[\varepsilon_{\mathrm{ct}} \frac{1+\xi}{\psi\xi} \left(\frac{1}{2\gamma}\right)^{\frac{1}{2\delta}}\right]^{\frac{2\delta}{\beta}} \tag{75}$$

Eqs. (72)–(75) are conceptually visualized in Fig. 7, providing two different conditions for the cracking response of a member. The continuous lines represent the steel strains, while the dashed lines represent the corresponding concrete strains. Note that the concrete

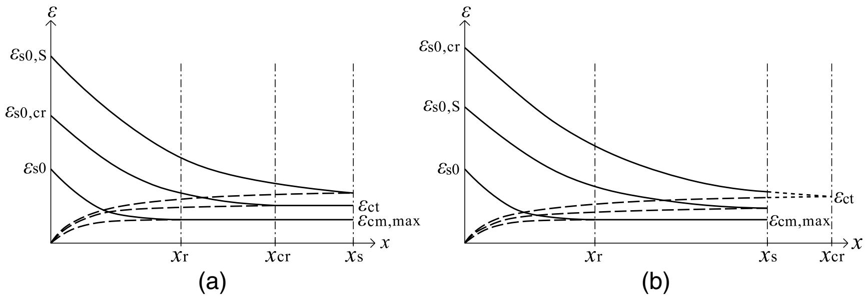

Fig. 7. (a) Condition 1; and (b) Condition 2.

strain for $\varepsilon_{s0,S}$ in Fig. 7(a) is unrealistic since the concrete tensile strength is exceeded. It is only included to elucidate the physical concept of Eq. (72). Condition 1 implies that a crack forms at a distance from the loaded end shorter than half the member length, i.e., $x_{cr} < x_S$, meaning that $\varepsilon_{s0,cr} < \varepsilon_{s0,S}$. This further implies that the cracking response of the member is governed by CLLM behavior as long $\varepsilon_{s0} < \varepsilon_{s0,cr}$, while CHLM behavior governs the cracking response as soon as $\varepsilon_{s0} > \varepsilon_{s0,cr}$. Condition 2 implies that a crack can form only at the symmetry section, $x_{cr} = x_s$, because $\varepsilon_{s0,cr} > \varepsilon_{s0,S}$. This means that a CLLM behavior governs the cracking response of the member as long $\varepsilon_{s0} < \varepsilon_{s0,S}$, while CHLM behavior governs the cracking response as soon $\varepsilon_{s0} > \varepsilon_{s0,S}$. The physical interpretation of Condition 1 is that cracking can form at any location beyond x_r due to the unrestricted length of the member, while Condition 2 means that cracking can form only at the symmetry section due to the limited length of the member. Appendix II provides guidelines for determining which condition applies and whether CLLM or CHLM behavior governs the cracking response based on the a priori loading and the mechanical properties of the RC tie. For design purposes, however, only Condition 1 is relevant for determining the cracking response.

Crack Width

Finally, the crack width is obtained as

$$w_{cr} = 2\int_{x_r} (\varepsilon_s - \varepsilon_{cm})dx \tag{76}$$

Inserting Eqs. (15), (44), and (45) in Eq. (76) yields

$$w_{cr} = 2\left(\frac{1}{1+\xi}\right)[\xi\varepsilon_{s0}x_r(1-\psi) + u_0(1+\psi\xi)] \tag{77}$$

In summary, the crack width is a function of the applied load $\varepsilon_{s0} = F/A_sE_s$, the transfer length x_r, and the slip at the loaded end u_0. For design purposes, i.e., Condition 1, the crack width is determined by calculating u_0 and x_r, which in the case of CLLM behavior is obtained by the closed-form solutions in Eqs. (50) and (51). A solution strategy is provided in subsection "Solution strategy" to calculate u_0 efficiently in the case of CHLM behavior, but here x_r is replaced with $x_{cr}/2$, where x_{cr} is the crack spacing obtained using the closed-form solution in Eq. (75). Note that the crack width obtained w_{cr} applies to the face at the loaded rebar end, i.e., as depicted in Fig. 1. This means that the calculation model conservatively assumes that a crack has been formed before loading, which allows for predicting crack widths regardless of the load level.

Comparison with Equivalent Calculation Models

The calculation model described was evaluated against the equivalent models proposed by Russo and Romano (1992), Balázs (1993), and Debernardi and Taliano (2016). The models are equivalent in the sense that the SODE for the slip, i.e., Eq. (34), is solved. However, some significant differences should be highlighted. The models of Balázs (1993) and Debernardi and Taliano (2016) neglect the elastic shear deformation over the cover, i.e., they assume $\psi = 1$ in Eq. (14). Another significant difference in Debernardi and Taliano (2016) is that the bond stress distribution over the bar length is altered locally by using a linear descending branch close to the primary crack, which complicates the solution of Eq. (34). These authors assume that internal inclined cracks form in this region and continue to form towards the symmetry section as the load increases. The FE analysis by Lutz (1970) and by Tan et al. (2018b) on RC ties show that a buildup of bond stresses occurs close to a primary crack and that the peak of the bond stress distribution tends to move towards the symmetry section as the load increases, as assumed by Debernardi and Taliano (2016). However, this physical phenomenon is a consequence not of internal inclined cracks, but of internal splitting cracks forming close to the primary crack, which is reflected by the characteristic bond-slip curves at $x \approx 0$ in Fig. 4. In fact, the FE analysis showed that internal inclined cracks also formed beyond the bond stress distribution peak, which means they cannot occur in direct conjunction with the descending branch alone. This also means that a single bond-slip curve should suffice to represent the mean local bond-slip behavior over the bar length, as shown in Fig. 4 and discussed in section "Physical Behavior of RC Ties," and should already include the total effect of both internal splitting and internal inclined cracks have on reducing the bond transfer.

The calculation model presented in this paper was particularly inspired by the work of Russo and Romano (1992). However, there are some significant differences: (1) a primary crack is assumed to form when, $\varepsilon_{cm} = \varepsilon_{ct}$, implying that concrete stresses are unevenly distributed even at the zero-slip section in accordance with the observations in Fantilli et al. (2007) and Tan et al. (2018c); (2) the influence of the distance between steel bars can be accounted for by Eq. (32); and (3) a completely analytical solution strategy is provided to solve Eq. (34) for practical applications. In addition, the derivations using continuum mechanics formulation yield a mechanically sound model that describes how the 3D behavior of RC ties can be simplified into a one-dimensional model when using a proper bond-slip law. However, the main advantage of the model presented in this paper, and that of Russo and Romano (1992), is that Eq. (34) is solved completely analytically, in contrast to Balázs (1993) and Debernardi and Taliano (2016), who only provide analytical solutions in the case of CLLM behavior.

Using the bond-slip curve recommended by Tan et al. (2018b) implies that the bond stresses should be related to the deformations in the outer surface of the concrete rather than at the steel-concrete interface, which contradicts the compatibility in Eq. (24). However, the elastic shear deformation over the cover is normally considered to be negligible, although it does seem to affect the elastic stress and strain distribution (Braam 1990; Tan et al. 2018c). This justifies the combined use of the chosen bond-slip curve, the compatibility in Eq. (24), and the concept of ψ in Eq. (14).

Application

Comparison with Axisymmetric RC Ties

General

This section compares strains and crack widths obtained analytically with the classical experiments of Bresler and Bertero (1968) and Yannopoulos (1989), and the FE analysis of Tan et al. (2018b) on cylindrical RC ties concentrically reinforced with a steel bar loaded at the steel bar ends. The bond-slip parameters, $\tau_{\max} = 5.0$ MPa, $u_1 = 0.1$ mm, and $\alpha = 0.35$ were chosen, while $\psi = 0.70$ was adopted in accordance with Tan et al. (2018c). The factor $\zeta = 1$ was chosen due to axisymmetry. The infinite series used for calculating the response in the case of CHLM behavior was truncated after 10 terms, while the parameters $\Delta x = 0.1$ and $du = 5.8 \cdot 10^{-5}$ were chosen in accordance with Russo and Romano (1992).

Comparison with Experimental Data

Bresler and Bertero (1968) measured the strain distribution over the bar length by mounting several strain gauges in a groove cut along the center of several reinforcing steel bars. The reinforcing steel bars were first cut longitudinally into two halves, after which the groove was milled along the center of the two parts. After mounting the strain gauges in this groove, the two halves were tack-welded together to minimize the impact on the exterior of the reinforcing bars. The specimen investigated, denoted *Specimen H*, was 406.4 mm (16 in.) long and 152.4 mm (6 in.) in diameter concentrically reinforced with a 28.7 mm (1.13 in.) deformed steel bar. The length of the specimen was chosen as twice the mean crack spacing of 203.2 mm (8 in.) obtained from pilot studies conducted on 1,829 mm (72 in.) long RC ties with similar sectional properties. A notch was cut around the circumference at midlength to induce cracking here. The compressive strength, tensile strength, and Young's modulus for the concrete were reported as respectively 40.8 MPa (5.92 ksi), 4.48 MPa (0.65 ksi), and 33165 MPa (4810 ksi), while the yield strength and Young's modulus for the steel were reported as 413 MPa (60 ksi) and 205,464 MPa (29,800 ksi), respectively. The reduction of the steel area due to the groove was taken into account in the analytical calculations by using the reported steel area $A_s = 548$ mm^2 (0.85 in.^{2}), while the notch was taken into account by reducing the reported tensile strength by a factor of 0.7. This led to cracking at midlength in the analytical calculations for higher load levels as shown in Fig. 8(a). It should be noted that the analytical steel strains represent the mean of the experimental steel strains.

The six specimens investigated by Yannopoulos (1989) were 76 mm in diameter concentrically reinforced with a 16 mm deformed steel bar and were 100 mm long. The length of the specimens was based on the mean crack spacing of 90 mm obtained from pilot studies conducted on 800 mm long RC ties with similar sectional properties and was chosen to prevent new cracks from forming between the loaded ends. The compressive strength, tensile strength, and Young's modulus for concrete were reported respectively as 43.4, 3.30, and 32,000 MPa, while the yield strength and Young's modulus for steel were reported as 424 and 200,000 MPa, respectively. The specimen length in the analytical calculations was chosen to be similar to that in the experiments. Fig. 8(b) shows the average crack width development at the loaded ends reported for the six specimens investigated. The analytical calculations predicted slightly larger crack widths. Nevertheless, the comparison shows good agreement.

Comparison with FE Analysis

Tan et al. (2018b) conducted NLFEA on four cylindrical RC ties denoted $\phi20c40$, $\phi32c40$, $\phi20c90$, and $\phi32c90$ using axisymmetric elements, with ϕ and c respectively indicating steel bar diameter and cover. The concrete was given material properties corresponding to a concrete grade C35 in accordance with MC2010 and a nonlinear fracture mechanics material model based on total strain formulation with rotating cracks. The crack bandwidth was chosen to be dependent on the total area of the finite elements in line with the smeared crack approach. The steel was chosen to have linear elastic material properties with a Young's modulus of 200,000 MPa and a Poisson's ratio of 0.3. Furthermore, interface elements were used to allow for radial separation but no physical slip, as depicted in Fig. 1(b). In summary, the approach implied smearing out internal inclined and splitting cracks that would have localized at the tip of each bar rib if they were modelled discretely. This was found to give good agreement in comparison with the steel strains, development of crack widths, and mean crack spacing observed in the experiments.

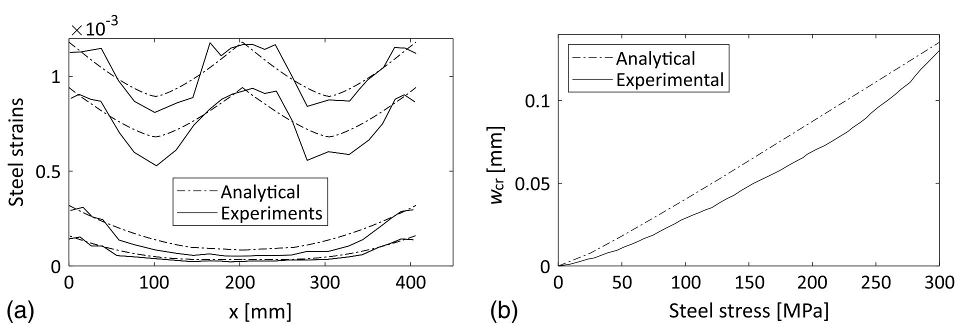

Fig. 8. (a) Comparison of steel strains predicted with steel strains reported in the experiments of Bresler and Bertero (1968) over the bar length; and (b) comparison of crack widths predicted with crack widths reported in the experiments of Yannopoulos (1989) using similar specimen length $L = 100$ mm similar to that in the experiments.

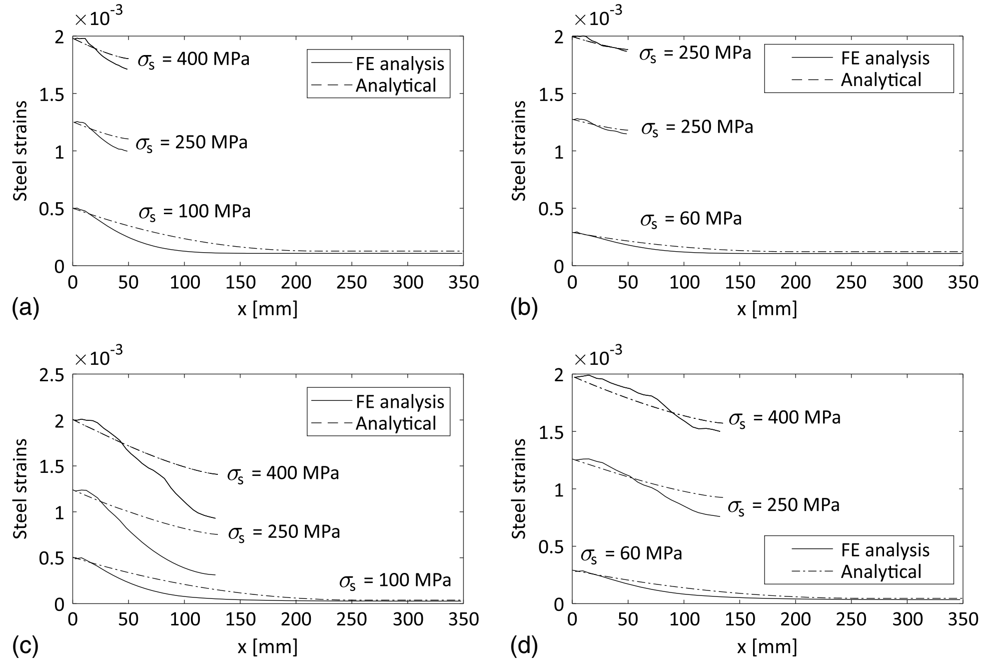

Fig. 9. Comparison of steel strains predicted with steel strains reported over the bar length in the FE analysis of Tan et al. (2018b): (a) specimen $\phi 20c40$; (b) specimen $\phi 32c40$; (c) specimen $\phi 20c90$; and (d) specimen $\phi 32c90$.

Fig. 9 shows the comparison of steel strain distributions over the bar lengths at three different stress levels for the specimens, again noting that the analytical model predicts the mean of the experimental steel strains. The first stress level shows the CLLM behavior just before a crack forms at a certain distance from the loaded end, while the two higher stress levels show the CHLM behavior for specimen lengths similar to the crack spacing obtained in the FE analysis (see Table 1). Note that the strain distribution is shown for only half the specimen length due to symmetry. In general, the analytical calculations make conservative predictions of the CLLM behavior, which also is reflected in the comparison of the predicted crack spacing in Table 1. The table also shows that the analytical model predicts crack spacing consistently and on the conservative side regardless of the bar diameter and cover size. The conservative prediction of the crack spacing can be attributed to the bond-slip parameters chosen. Fig. 10 shows the development of crack widths in specimens with lengths similar to the FE analysis crack spacing in Table 1 and indicates that the analytical model makes quite accurate predictions of crack widths for a given specimen length.

Fig. 11 shows comparisons of the development of crack widths based on specimen lengths similar to the crack spacing predicted by the analytical model in Table 1. The analytical model yields Condition 2 and CHLM behavior in general, which allows for cracking at midlength at higher load levels and occurs for all of the specimens except $\phi 20c90$. The graphs also show that the analytical model predicts crack widths on the conservative side in general.

Table 1. Comparison of crack spacing predicted with mean crack spacing reported in the experiments of Bresler and Bertero (1968) and Yannopoulos (1989), and the FE analysis of Tan et al. (2018b)

RC tie	Experimental and FE analysis mean (mm)	Predicted analytical (mm)
Bresler and Bertero (1968)	203	301
Yannopoulos (1989)	90	181
$\phi 20c40$	105	224
$\phi 32c40$ Tan et al. (2018b)	109	207
$\phi 20c90$	260	470
$\phi 32c90$	272	434

Comparison with Nonaxisymmetric RC Ties

The French research project CEOS.fr (2016) conducted experiments on two identical quadratic RC ties identified as Ties 4 and 5, which were pulled in tension. The ties were 355 mm in width and height, had a length of 3,200 mm, and were reinforced with eight 16 mm rebars. A concrete grade C40/50 was used, while the yield strength and Young's modulus of steel were reported as 529 and 200,000 MPa, respectively. The cover to the rebars was 45 mm. Fig. 12(a) shows a comparison of the development of predicted crack widths with the maximum crack widths measured. The analytical calculations were based on using specimen lengths similar to the crack spacing predicted analytically in Table 2. The factor $\zeta = 1$ was chosen for simplicity. The deviation between Ties 4 and 5 in the maximum crack widths measured seems to be due to the difference in maximum crack spacing reported in Table 2. Nevertheless, the maximum crack spacing predictions were conservative, and the crack widths predicted show relatively good agreement with the maximum crack widths measured.

Tan et al. (2018a) conducted experiments on eight quadratic RC ties identified as X-ϕ-c, where X represents the loading regime the RC tie was exposed to, either at the crack formation stage (F) or the stabilized cracking stage (S), while ϕ and c represent the rebar diameter and cover respectively. The rebar diameter was either 20 or 32 mm, while the cover was either 40 or 90 mm. The ties were 400 mm in width and height, had a length of 3000 mm, and were reinforced with eight rebars. The concrete compressive and tensile strength were reported as 74.3 and 4.14 MPa, respectively, while the Young's modulus was reported as 27.4 MPa. The yield strength and Young's modulus of the steel were reported as 500 and 200,000 MPa, respectively. Fig. 12(b) shows the comparison

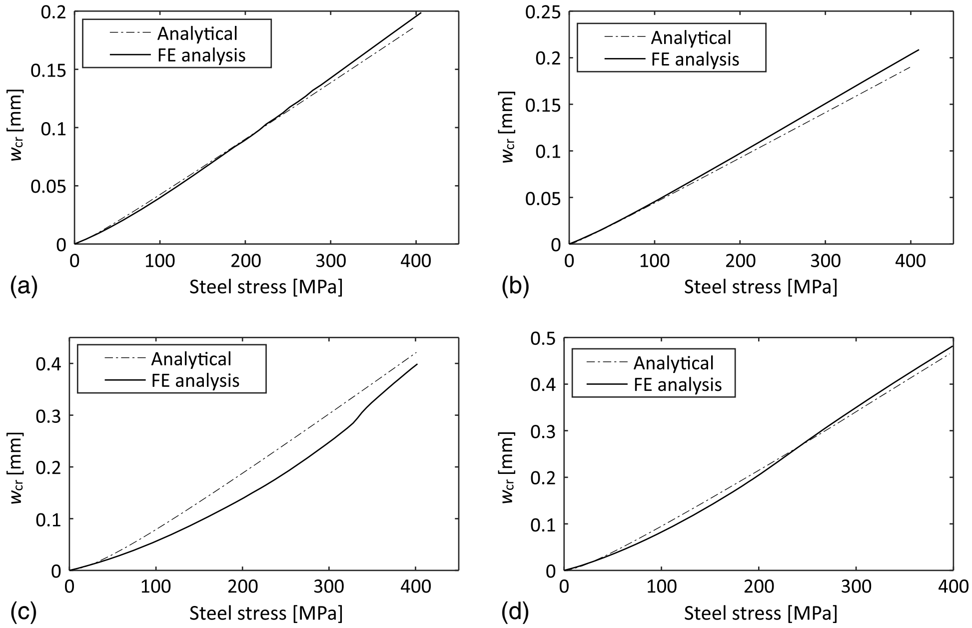

Fig. 10. Comparison of crack widths predicted (in specimens with lengths similar to FE analysis mean crack spacing reported in Table 1 with crack widths reported in the FE analysis of Tan et al. (2018b); (a) specimen $\phi 20c40$, $L = 105$ mm; (b) specimen $\phi 32c40$, $L = 109$ mm; (c) specimen $\phi 20c90$, $L = 260$ mm; and (d) specimen $\phi 32c90$, $L = 272$ mm.

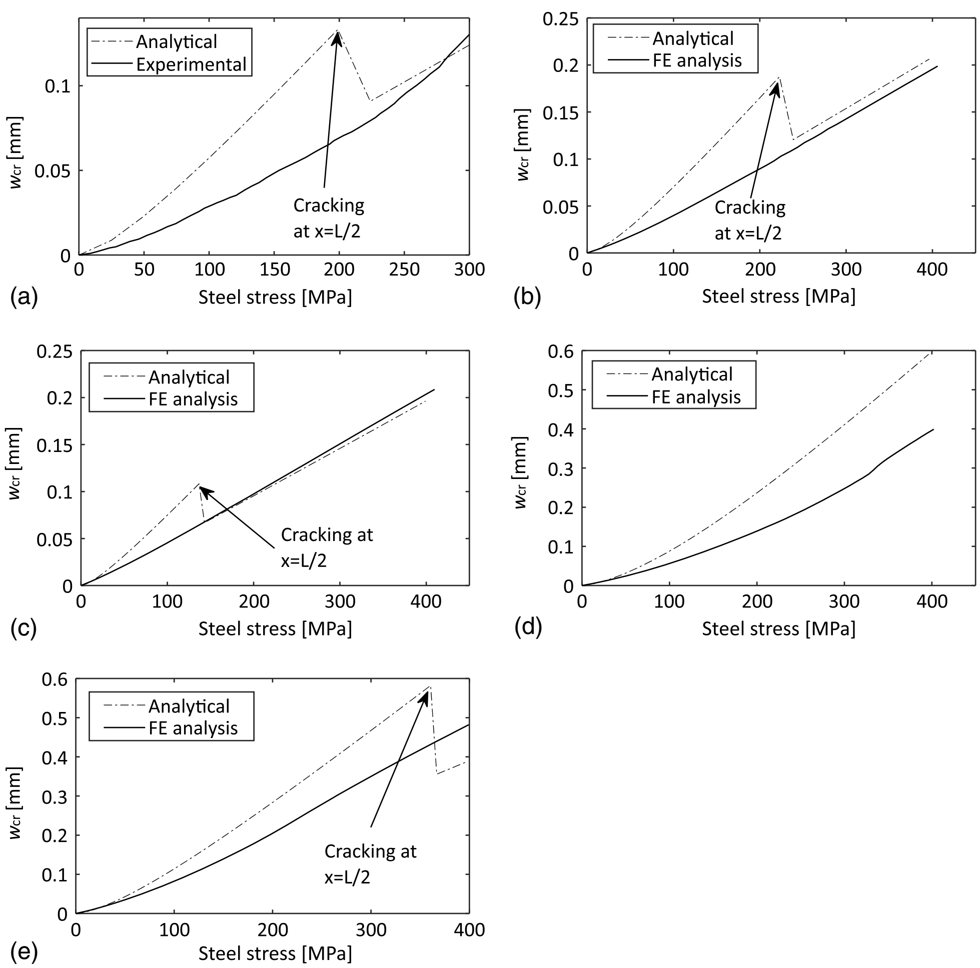

Fig. 11. Comparison of crack widths predicted (in specimens with lengths similar to crack spacing predicted in Table 1 with crack widths reported in the experiments of Yannopoulos (1989) and the FE analysis of Tan et al. (2018b): (a) Yannopoulos (1989) specimen, $L = 181$ mm; (b) specimen $\phi 20c40$, $L = 224$ mm; (c) specimen $\phi 32c40$, $L = 207$ mm; (d) specimen $\phi 20c90$, $L = 470$ mm; and (e) specimen $\phi 32c90$, $L = 434$ mm.

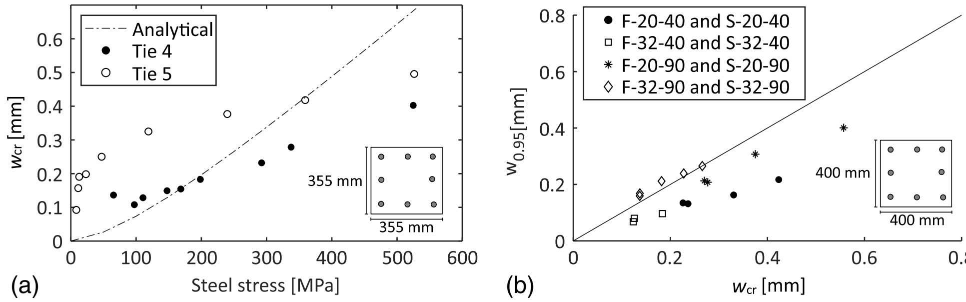

Fig. 12. Comparison of crack widths predicted (in specimens with lengths similar to crack spacing predicted in Table 2) with crack widths reported in experiments: (a) CEOS.fr (2016); and (b) Tan et al. (2018a).

Table 2. Comparison of crack spacing predicted with crack spacing reported in the experiments of CEOS.fr (2016) and Tan et al. (2018a)

RC tie	Study	Experimental Mean (mm)	Experimental Maximum (mm)	Predicted analytical (mm)
Tie 4	CEOS.fr (2016)	160	257	370
Tie 5	—	188	318	370
S-20-40	—	163	250	422
S-32-40	Tan et al. (2018a)	178	240	361
S-20-90	—	217	290	422
S-32-90	—	266	320	361

of maximum crack widths measured $w_{0.95}$ and crack widths predicted w_{cr} using the concept of modelling uncertainty, i.e., as $\theta = w_{0.95}/w_{\mathrm{cr}}$. The crack widths calculated were based on using specimen lengths similar to the crack spacing predicted analytically in Table 2. The factor $\zeta = 1$ was again chosen for simplicity. Both the crack widths and the crack spacing predicted are on the conservative side except for F-32-90 and S-32-90, in which the maximum crack widths predicted were slightly underestimated.

Discussion

The conservative predictions of the crack widths in Fig. 11 are due to the nature of Eq. (75), which, together with the predefined bond-slip parameters, provides an upper limit for the crack spacing or, expressed more rigorously, for the maximum crack spacing. This is equivalent to the concept of calculating the maximum crack widths according to the semiempirical formulas in EC2 and MC2010. However, unlike EC2 and MC2010, Eq. (75) is not assumed to vary from once to twice this value. Furthermore, Figs. 8(b) and 10 show the ability of the model to predict accurate crack widths given a specimen length. The observations in Figs. 8(a) and 9 suggest that the analytical model can predict the mean behavior of experimental steel strains, which is a direct result of using just one local bond-slip curve to represent the bond transfer over the specimen length. This means that the effect internal inclined and splitting cracks has on reducing the bond transfer locally is smeared over the specimen length in the analytical model. The consequence of using only one local bond-slip curve is that the bond stresses reach their maximum at the cracked section ($x = 0$), which contradicts the physical behavior of RC ties discussed previously. This is because the selected bond-slip curve causes bond stresses to increase with increasing slip as can be observed in Fig. 4. This is elucidated in Fig. 13, which shows the corresponding bond stresses to the steel strains predicted in Fig. 9. One solution to this problem would be to use different bond-slip curves depending on the location over the specimen length, but this would substantially complicate the solutions to the analytical model. So, the use of just one local bond-slip curve provides a practical yet mechanically sound calculation model that has proven capable of predicting the development of crack widths and crack spacing consistently and on the conservative side, regardless of the mechanical properties and loading of the RC ties. Another advantage of using a bond-slip curve, as opposed to assuming a constant bond stress distribution e.g., in EC2 and MC2010, is that the mean bond stresses become dependent on the load level and the geometry of RC tie, thus conforming to the theoretical observations made by Tan et al. (2018b). This should provide more realistic predictions of the crack spacing.

Fig. 14 shows the corresponding concrete strains at the interface, $\varepsilon_{\mathrm{ci}}$, to the steel strains predicted in Fig. 9 at load levels 250 and 400 MPa, whereas the dashed lines represent the resultant of concrete strains in a section according to Eq. (15), i.e., as $\varepsilon_{\mathrm{cm}} = \psi\varepsilon_{\mathrm{ci}}$. It is observed that both the concrete stresses at the interface and the resultants of concrete stresses increase with increasing load level. This is due to the increase of the bond transfer between the load levels of 250 and 400 MPa as represented by the increase of the areas under the curves shown in Fig. 13. Furthermore, this would cause a crack to form at the zero-slip section even in the case of CHLM behavior if the mean concrete strains exceed the tensile strength of concrete, as shown in Fig. 11. This conforms to the discussions of transient cracking of RC ties addressed in *fib* bulletin No. 10 (*fib* 2000). This feature though, can easily be neglected in the calculation model for design situations as a conservative approach. The main reason for including ψ in Eq. (14) was to account for the fact that nonlinear strain profiles occur over the concrete cover (Tan 2018c), which is a mechanical improvement to the assumption of claiming that plane sections remain plane in RC ties as per (Saliger 1936; Balázs 1993; CEN 2004; *fib 2013*; Debernardi and Taliano 2016). It can be shown though, that different values of ψ in general have limited effect on the crack width predictions.

Fig. 12 shows that the analytical model presented can be applied to predict crack widths in nonaxisymmetric RC ties as well. In these calculations, simple assumptions were made such as that the whole concrete area contributed in tension $A_{\mathrm{c,ef}} = A_{\mathrm{c}}$ and choosing $\zeta = 1$. This led to similar crack spacing predictions for RC ties with similar reinforcement ratios but different covers, which contradicts the experimental data in Table 2. It is well known that the cover has a significant influence on crack spacing, and therefore crack widths, as reported by Broms (1968), Gergely and Lutz (1968), Caldentey et al. (2013), and Tan et al. (2018a). One approach to taking the cover into account could be to use the provisions in EC2 and MC2010 for calculating an effective reinforcement ratio, $\rho_{\mathrm{s,ef}} = A_{\mathrm{s}}/A_{\mathrm{c,ef}}$,

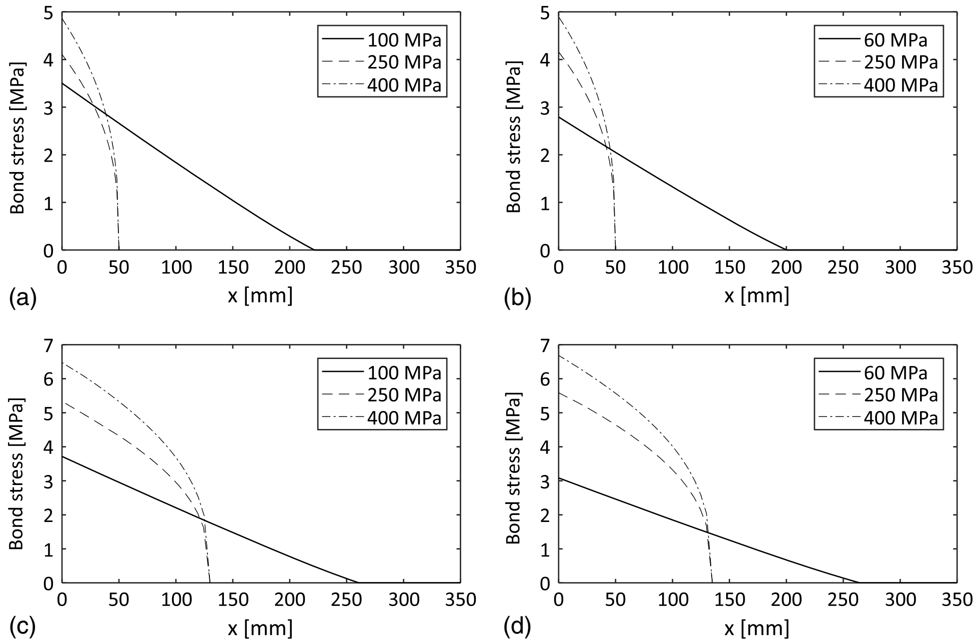

Fig. 13. Bond stresses corresponding to the steel strains predicted in Fig. 9: (a) specimen $\phi 20c40$; (b) specimen $\phi 32c40$; (c) specimen $\phi 20c90$; and (d) specimen $\phi 32c90$.

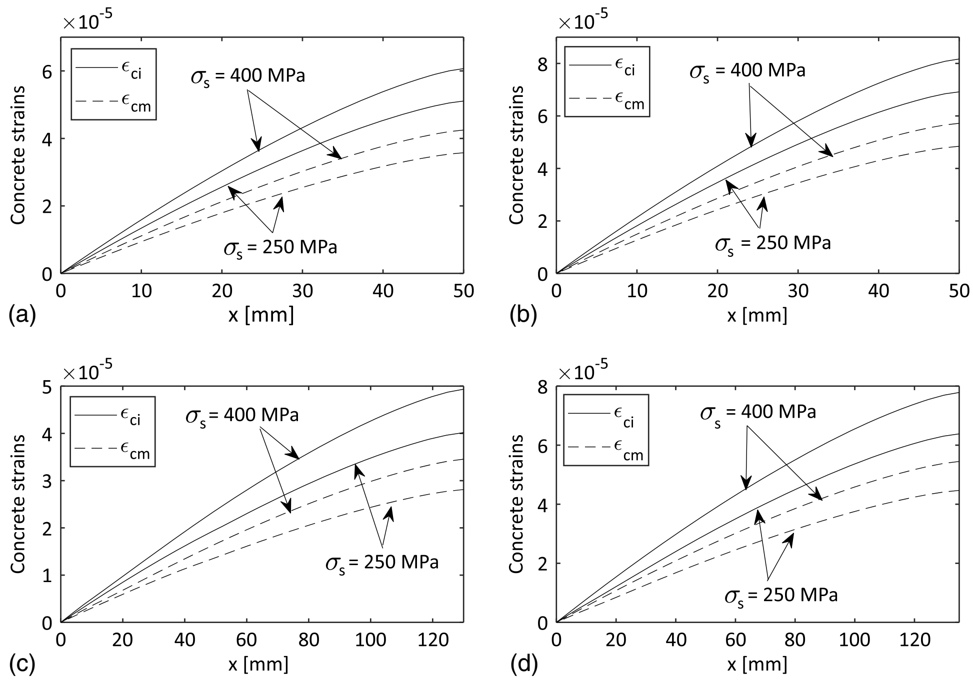

Fig. 14. Concrete strains corresponding to the steel strains predicted in Fig. 9: (a) specimen $\phi 20c40$; (b) specimen $\phi 32c40$; (c) specimen $\phi 20c90$; and (d) specimen $\phi 32c90$.

to predict the cracking behavior. This is exemplified in Table 3, which shows the crack spacing predictions when the effective height surrounding the rebars, i.e., $h_{\mathrm{c,ef}} = \min[2.5(c + \phi/2), h/2]$, is used to determine the effective reinforcement ratios. Comparison of specimens having similar geometrical reinforcement ratios, e.g., S-20-40 against S-20-90 and S-32-40 against S-32-90, shows that the crack spacing predictions increase for specimens having larger covers owing to the difference in effective reinforcement ratios. However, the increase in crack spacing predictions for specimens with larger

Table 3. Comparison of crack spacing reported in the experiments of Tan et al. (2018a) and crack spacing predicted using effective reinforcement ratios

RC tie	Experimental: Mean (mm)	Experimental: Maximum (mm)	Predicted analytical (mm)
S-20-40	163	250	390
S-32-40	178	240	342
S-20-90	217	290	422
S-32-90	266	320	361

covers is seen to be underestimated compared to the experimental evidence. This could also be related to assuming $\zeta = 1$, which is questionable particularly for RC ties with 90 mm cover because the bond stress distribution surrounding the perimeter of the rebars is probably not uniform, as elucidated in Fig. 2(d). However, determining a proper value for ζ is not straightforward and requires further study, e.g., by conducting FE analysis of nonaxisymmetric RC ties. Nevertheless, the model with the introduction of the factor ζ and an effective reinforcement ratio based on the cover size shows great potential in predicting the cracking behavior of nonaxisymmetric RC ties as well.

The calculation model using the simplified equations for concrete can predict crack widths both in the *crack formation stage* and the *stabilized cracking stage* through the concepts of CLLM and CHLM, and is as such different from the calculation methods recommended by EC2 and MC2010, which apply to the stabilized cracking stage only. Furthermore, assuming ψ not equal to one implies that the mean concrete strains over the section in general is different from the concrete strains at the interface further implying that the concrete stresses in each section are assumed unevenly distributed, even at the zero-slip section, a concept first introduced by Edwards and Picard (1972). This means that a crack forms when the resultant of concrete stresses at the zero-slip section is equal to the mean value of the tensile strength as pointed out for Eq. (74). Finally, using only one bond-slip curve means that bond stresses are different from null at the cracked section. These assumptions enabled a practical approach to solve the SODE for the slip.

The model allows for treating problems such as *imposed deformations*, where the mechanical loading becomes directly dependent on the crack pattern or, expressed more rigorously, the stiffness of the member. Moreover, the authors of this paper are also currently working on the application of the analytical model to more general cases, such as noncylindrical RC ties, tensile zones in structural elements exposed to bending, and RC membrane elements exposed to biaxial stress states at which cracks form at a skew angle to an orthogonal reinforcement grid.

Conclusions

A new analytical crack width calculation model has been formulated to provide more consistent crack width calculations for large-scale concrete structures, where large covers and bar diameters are typically used. The calculation model was derived based on the uniaxial behavior of axisymmetric RC ties. Furthermore, the model includes the effect of internal cracking on the bond transfer, a nonuniform strain distribution over the concrete area and a nonuniform bond stress distribution surrounding the perimeter of the steel bar in nonaxisymmetric cases. The latter accounts for the effect of steel bar spacing in practice.

The SODE for the slip has been solved completely analytically, yielding closed-form solutions in the case of CLLM behavior and non-closed-form solutions in the case of CHLM behavior. One solution strategy and method for determining the complete cracking response has been provided for the purposes of facilitating a practical applicable calculation model, the lack of which has been the major drawback in using previous equivalent models. The comparison with experimental and finite-element results in the literature shows that the calculation model predicts an average strain distribution based on using a single local bond-slip curve to represent the bond transfer. The comparisons demonstrate the ability of the calculation model to predict crack widths accurately given a member length. Finally, the model has proven capable of predicting crack spacing and crack widths consistently and in general on the conservative side regardless of the bar diameter and cover, even for nonaxisymmetric RC ties.

Appendix I. Function Derivatives for CHLM

Function derivatives in the case of CHLM behavior for Case 1.

$$f_1'(u_0) = -\frac{1}{\sqrt{2}}\sum_{k=0}^{\infty}\begin{pmatrix}-\frac{1}{2}\\ k\end{pmatrix}\gamma^k\left[\gamma\beta u_0^{\beta-1}\left(\frac{1}{2}+k\right)C^{-\frac{3}{2}-k}\frac{u_0^{1+k\beta}}{1+k\beta}+C^{-\left(\frac{1}{2}+k\right)}u_0^{k\beta}\right] \tag{78}$$

Function derivatives in the case of CHLM behavior for Case 2.

$$f_2'(u_0) = -\frac{1}{\sqrt{2\gamma}}[f_{21}'(u_0)-f_{22}'(u_0)]-\frac{1}{\sqrt{2}}f_{23}'(u_0) \tag{79}$$

$$f_{21}'(u_0) = \sum_{k=0}^{\infty}\begin{pmatrix}-\frac{1}{2}\\ k\end{pmatrix}\left(\frac{1}{\gamma}\right)^k\left[C^k u_0^{\delta-k\beta-1}-\frac{\gamma\beta kC^{k-1}}{\delta-k\beta}u_0^{\beta(1-k)+\delta-1}\right] \tag{80}$$

$$f_{22}'(u_0) = \sum_{k=0}^{\infty}\begin{pmatrix}-\frac{1}{2}\\ k\end{pmatrix}\left[\left(\frac{C}{\gamma}\right)^{\frac{k}{\delta-k\beta}+\frac{1}{\beta}}+du\left(\frac{C}{\gamma}\right)^{\frac{k}{\delta-k\beta}}\right]^{\delta-k\beta-1}\cdot(-\gamma\beta u_0^{\beta-1})\cdot\left[\left(\frac{1}{\gamma}\right)^{\frac{k}{\delta-k\beta}+\frac{1}{\beta}}\left(\frac{k}{\delta-k\beta}+\frac{1}{\beta}\right)C^{\frac{k}{\delta-k\beta}+\frac{1}{\beta}-1}+du\left(\frac{1}{\gamma}\right)^{\frac{k}{\delta-k\beta}}\left(\frac{k}{\delta-k\beta}\right)C^{\frac{k}{\delta-k\beta}-1}\right] \tag{81}$$

$$f_{23}'(u_0) = \sum_{k=0}^{\infty}\begin{pmatrix}-\frac{1}{2}\\ k\end{pmatrix}\gamma^k\left[\left(\frac{1}{\gamma}\right)^{\frac{1}{\beta}}C^{\frac{2-\beta}{2\beta(1+k\beta)}}-duC^{-\frac{\frac{1}{2}+k}{1+k\beta}}\right]^{k\beta}\cdot(-\gamma\beta u_0^{\beta-1})\cdot\left\{\left(\frac{1}{\gamma}\right)^{\frac{1}{\beta}}\left[\frac{2-\beta}{2\beta(1+k\beta)}\right]C^{\left[\frac{2-\beta}{2\beta(1+k\beta)}-1\right]}+du\left[\frac{\frac{1}{2}+k}{1+k\beta}\right]C^{-\left[\frac{\frac{1}{2}+k}{1+k\beta}+1\right]}\right\} \tag{82}$$

J. Struct. Eng., 2020, 146(2): 04019206

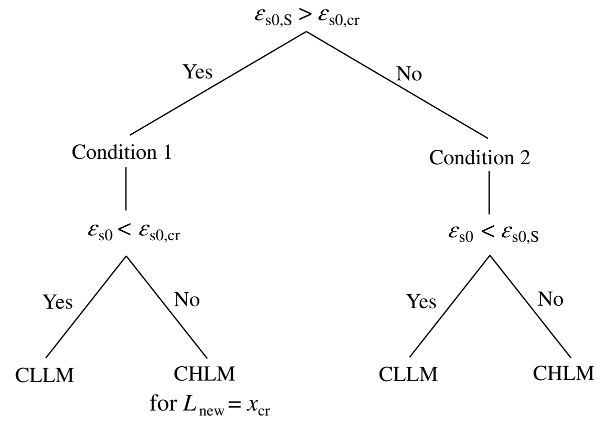

Fig. 15. Flowchart for determining the cracking response a priori.

Appendix II. Procedure to Determine the Cracking Response

A method for determining the complete cracking response is shown in Fig. 15, in which $\varepsilon_{s0,s}$, $\varepsilon_{s0,cr}$, and x_{cr} are determined by Eqs. (72), (74), and (75) respectively, while ε_{s0} is the steel strain at the loaded end.

Acknowledgments

The work presented in this paper is part of an ongoing Ph.D. study funded by the Norwegian Public Roads Administration as a part of the Coastal Highway Route E39 project.

References

Balázs, G. L. 1993. "Cracking analysis based on slip and bond stresses." *ACI Mater. J.* 90 (4): 340–348.

Beeby, A. W. 2004. "The influence of the parameter φ/ρ_{eff} on crack widths." *J. Struct. Concr.* 5 (2): 71–83. https://doi.org/10.1680/stco.2004.5.2.71.

Borosnyói, A., and I. Snóbli. 2010. "Crack width variation within the concrete cover of reinforced concrete members." *Építőanyag* 62 (3): 70–74. https://doi.org/10.14382/epitoanyag-jsbcm.2010.14.

Borosnyói, B., and G. L. Balázs. 2005. "Models for flexural cracking in concrete: The state of the art." *J. Struct. Concr.* 6 (2): 53–62. https://doi.org/10.1680/stco.2005.6.2.53.

Braam, C. R. 1990. "Control of crack width in deep reinforced concrete beams." Ph.D. thesis, Faculty of Civil Engineering, Delft Univ. of Technology.

Bresler, B., and V. V. Bertero. 1968. "Behavior of reinforced concrete under repeated load." *J. Struct. Div.* 94 (6): 1567–1590.

Broms, B. 1968. "Theory of the calculation of crack width and crack spacing in reinforced concrete members." [In Swedish.] *Cem. Betong* 1: 52–64.

Caldentey, A. P., H. C. Peiretti, J. P. Iribarren, and A. G. Soto. 2013. "Cracking of RC members revisited: Influence of cover, $\phi/\rho_{s,ef}$ and stirrup spacing: An experimental and theoretical study." *J. Struct. Concr.* 14 (1): 69–78. https://doi.org/10.1002/suco.201200016.

CEN (European Committee for Standardization). 2004. *Eurocode 2: Design of concrete structures: Part 1-1: General rules and rules for buildings*. EN 1992-1-1. Brussels, Belgium: CEN.

CEOS.fr. 2016. *Control of cracking in reinforced concrete structures*. London: ISTE.

Debernardi, P. G., and M. Taliano. 2016. "An improvement to Eurocode 2 and *fib* model code 2010 methods for calculating crack width in RC structures." *Struct. Concr.* 17 (3): 365–376. https://doi.org/10.1002/suco.201500033.

Dörr, K. 1978. "Bond-behaviour of ribbed reinforcement under transversal pressure." In *Proc., IASS Symposium on Nonlinear Behaviour of Reinforced Concrete Spatial Structures*, 13–24. Düsseldorf, Germany: Werner Verlag.

Edwards, A. D., and A. Picard. 1972. "Theory of cracking in concrete members." *J. Struct. Div.* 98 (12): 2687–2700.

Eligehausen, R., E. P. Popov, and V. V. Bertero. 1983. *Local bond stress-slip relationships of deformed bars under generalized excitations: Experimental results and analytical model*. Rep. No. UCB/EERC 83/23. Berkeley, CA: Univ. of California.

Fantilli, A. P., H. Mihashi, and P. Vallini. 2007. "Crack profile in RC, R/FRCC and R/HPFRCC members in tension." *Mater. Struct.* 40 (10): 1099–1114. https://doi.org/10.1617/s11527-006-9208-7.

fib. 2000. *Bond of reinforcement in concrete: State-of-the-art report*. *fib* Bulletin No. 10. Lausanne, Switzerland: Sprint-Druck Stuttgart.

fib. 2013. *fib model code for concrete structures 2010*. Berlin: International Federation for Structural Concrete, Ernst & Sohn.

Gergely, P., and L. A. Lutz. 1968. *Maximum crack width in reinforced concrete flexural members*. Farmington Hills, MI: American Concrete Institute.

Goto, Y. 1971. "Crack formed in concrete around deformed tension bars." *ACI J.* 68 (4): 244–251.

Hong, S., and S. K. Park. 2012. "Uniaxial bond stress-slip relationship of reinforcing bars in concrete." *Adv. Mater. Sci. Eng.* 2012 (1): 328570. https://doi.org/10.1155/2012/328570.

Husain, S. I., and P. M. Ferguson. 1968. *Flexural crack width at the bars in reinforced concrete beams*. Research Rep. No. 102-1F. Austin, TX: Center for Highway Research, Univ. of Texas.

Irgens, F. 2008. *Continuum mechanics*. Bergen, Norway: Springer.

Kaklauskas, G. 2017. "Crack model for RC members based on compatibility of stress-transfer and mean-strain approaches." *J. Struct. Eng.* 143 (9): 04017105. https://doi.org/10.1061/(ASCE)ST.1943-541X.0001842.

Leonhardt, F. 1988. "Cracks and crack control in concrete structures." *PCI J.* 33 (4): 124–145. https://doi.org/10.15554/pcij.07011988.124.145.

Lutz, L. A. 1970. "Analysis of stresses in concrete near a reinforcing bar due to bond and transverse cracking." *ACI J.* 67 (10): 778–787.

Martin, H. 1973. "On the interrelation among surface roughness, bond and bar stiffness in the reinforcement subject to short-term loading." [In German.] *Deutscher Ausschuss Stahlbeton* 228: 1–50.

Mirza, S. M., and J. Houde. 1979. "Study of bond stress-slip relationships in reinforced concrete." *ACI J.* 76 (1): 19–46.

Nilson, A. H. 1972. "Internal measurement of bond slip." *ACI J.* 69 (7): 439–441.

NPRA (Norwegian Public Roads Administration). 2015. *N400 Bruprosjektering: Prosjektering av bruer, ferjekaier og andre bærende konstruksjoner: N400 in Statens vegvesens håndbokserie*. Oslo, Norway: Statens Vegvesen.

Pedziwiatr, J. 2008. "Influence of internal cracks on bond in cracked concrete structures." *Arch. Civil Mech. Eng.* 8 (3): 91–105. https://doi.org/10.1016/S1644-9665(12)60165-4.

Rehm, G. 1961. "On the fundamentals of the steel-concrete bond." [In German.] *Deutscher Ausschuss für Stahlbeton* 138: 1–59.

Russo, G., and F. Romano. 1992. "Cracking response of RC members subjected to uniaxial tension." *J. Struct. Eng.* 118 (5): 1172–1190. https://doi.org/10.1061/(ASCE)0733-9445(1992)118:5(1172).

Russo, G., G. Zingone, and F. Romano. 1990. "Analytical solution for bond-slip of reinforcing bars in R.C. joints." *J. Struct. Eng.* 116 (2): 336–355. https://doi.org/10.1061/(ASCE)0733-9445(1990)116:2(336).

Saliger, R. 1936. "High-grade steel in reinforced concrete." In *Proc., 2nd Congress of the Int. Association for Bridge and Structural Engineering*, 293–315. Zurich, Switzerland: ETH Zürich.

Tammo, K., and S. Thelandersson. 2009. "Crack behavior near reinforcing bars in concrete structures." *ACI Struct. J.* 106 (3): 259–267.

Tan, R., K. Eileraas, O. Opkvitne, G. Žirgulis, M. A. Hendriks, M. Geiker, D. E. Brekke, and T. Kanstad. 2018a. "Experimental and theoretical investigation of crack width calculation methods for RC ties." *Struct. Concr.* 19 (5): 1436–1447. https://doi.org/10.1002/suco.201700237.

Tan, R., M. A. N. Hendriks, M. Geiker, and T. Kanstad. 2018b. "A numerical investigation of the cracking behaviour of reinforced concrete tie elements." *Mag. Concr. Res.* https://doi.org/10.1680/jmacr.18.00156.

Tan, R., M. A. N. Hendriks, and T. Kanstad. 2018c. "An investigation of the strain profile over the cover in reinforced concrete elements subjected to tension." In *Proc., fib Congress*. Melbourne, Australia: FIB Congress 2018.

Watstein, D., and R. G. Mathey. 1959. "Width of cracks in concrete at the surface of reinforcing steel evaluated by means of tensile bond specimens." *ACI J.* 56 (7): 47–56.

Yannopoulos, P. J. 1989. "Variation of concrete crack widths through the concrete cover to reinforcement." *Mag. Concr. Res.* 41 (147): 63–68. https://doi.org/10.1680/macr.1989.41.147.63.